

# Multi-probe analysis of strong-field effects in $f(Q)$ gravity

Mohsen Khodadi,<sup>1,2,\*</sup> Behnam Pourhassan,<sup>1,†</sup> and Emmanuel N. Saridakis<sup>3,4,5,‡</sup>

<sup>1</sup>*School of Physics, Damghan University, Damghan 3671641167, Iran*

<sup>2</sup>*Center for Theoretical Physics, Khazar University, 41 Mehseti Str., AZ1096 Baku, Azerbaijan*

<sup>3</sup>*The National Observatory of Athens, Lofos Nymfon 11852, Greece*

<sup>4</sup>*Departamento de Matemáticas, Universidad Católica del Norte,  
Avda. Angamos 0610, Casilla 1280, Antofagasta, Chile*

<sup>5</sup>*CAS Key Laboratory for Research in Galaxies and Cosmology, School of Astronomy and Space Science,  
University of Science and Technology of China, Hefei 230026, China*

Covariant  $f(Q)$  gravity is a viable extension of General Relativity, however its strong-field predictions remain largely untested. Using the static, spherically symmetric black-hole solutions of the theory, we confront it with the most stringent probes available: black-hole shadows, Event Horizon Telescope (EHT) measurements, S2-star precession, and strong gravitational lensing. We show that the two admissible solution branches behave very differently: Case I produces negligible deviations from Schwarzschild solution, whereas Case II yields significant, potentially observable corrections to the photon sphere and shadow size. From the EHT shadow diameters of M87\* and Sgr A\*, we obtain tight bounds, which are further strengthened by strong-lensing coefficients. These results provide the sharpest strong-field constraints on covariant  $f(Q)$  gravity to date, and point toward future tests using next-generation horizon-scale imaging and precision Galactic-center astrometry.

PACS numbers: 04.50.Kd, 98.80.-k, 04.80.Cc, 95.10.Ce, 96.30.-t

## I. INTRODUCTION

The discovery of the late-time universe acceleration has motivated the systematic research of modified gravity theories as alternatives to the standard  $\Lambda$ CDM scenario [1, 2]. Hence, in the literature one can find various extensions and modifications of General Relativity (GR). The simplest way to obtain them is by extending the usual Einstein-Hilbert action, resulting in  $f(R)$  gravity [3–5],  $f(G)$  gravity [6, 7], cubic gravity [8], Lovelock gravity [9, 10], or scalar-tensor theories such as Horndeski gravity [11–13] and generalized Galileon theory [14]. Nevertheless, one can start from the equivalent torsional formulation of gravity, and extend it in similar ways, obtaining  $f(T)$  gravity [15–17],  $f(T, T_G)$  gravity [18, 19], and  $f(T, B)$  gravity [20, 21], scalar-torsion theories [22], Teleparallel Equivalent of Horndeski theories [23–27], etc.

More recently, Nester [28] proposed a third geometric description of gravity, known as symmetric teleparallel gravity, in which the gravitational interaction is attributed entirely to non-metricity, distinct from curvature-based GR and torsion-based teleparallelism. This formulation has attracted considerable interest as an alternative foundation for constructing modified gravity models. Among these,  $f(Q)$  gravity is applied as one of the usual generalizations [29, 30], promoting the Lagrangian from its linear form to a general function  $f(Q)$ . This extension improves significantly the theory's phenomenology and has been applied in diverse settings, in-

cluding cosmological dynamics, astrophysical modeling, and static spherically symmetric spacetimes [31–45] (for a review see [46]).

A particularly convenient feature of standard  $f(Q)$  gravity is the Coincident Gauge (CG), which allows choosing coordinates in which the affine connection vanishes. However, although the CG simplifies calculations significantly, it faces severe limitations in the context of spherically symmetric spacetimes: the field equations collapse to linear form, preventing non-trivial  $f(Q)$  black hole solutions [47]. This issue has been resolved within the covariant formulation of  $f(Q)$  gravity [48], where the connection is allowed to be non-vanishing and symmetric. The impact of different affine connections on cosmological dynamics was further studied in [49–51].

While  $f(Q)$  gravity is strongly motivated by its success in explaining cosmological dynamics, a complete assessment of its viability requires confronting the theory with strong-field observations, where nonlinear gravitational effects dominate. Such environments offer independent and complementary tests to cosmology, since even small modifications of the metric can produce measurable deviations near compact objects. Recent efforts have begun to explore this regime through neutron-star structure [52], black-hole solutions [53], and gravitational-wave propagation [54, 55]. These studies emphasize that examining the theory under extreme conditions is essential both for identifying potential departures from GR and for breaking degeneracies that remain unresolved at low curvature.

Among all strong-field systems, black holes provide the most powerful and cleanest probes of high-curvature physics. The horizon-scale images of M87\* [56, 57] and Sgr A\* [58] obtained by the Event Horizon Telescope (EHT) have opened a new era of precision tests of grav-

\*Electronic address: [m.khodadi@du.ac.ir](mailto:m.khodadi@du.ac.ir)

†Electronic address: [b.pourhassan@du.ac.ir](mailto:b.pourhassan@du.ac.ir)

‡Electronic address: [msaridak@noa.gr](mailto:msaridak@noa.gr)

ity in the immediate vicinity of the photon sphere. These observations have already stimulated a vast body of work exploring horizon-scale phenomenology across different modified-gravity models [59–89]. In the context of covariant  $f(Q)$  gravity, static and spherically symmetric black-hole spacetimes can be constructed by adopting appropriate non-vanishing symmetric connections, as proposed in [90]. However, a systematic confrontation of these solutions with the expanding set of strong-field observables, including EHT shadows, stellar orbital dynamics, and strong gravitational lensing, remains absent from the literature.

In this work, we provide the first comprehensive strong-field test of power-law  $f(Q)$  gravity, which serves as a robust approximation to general viable  $f(Q)$  models. We derive and analyze the black-hole solutions associated with different symmetric connections, we study their photon-sphere and shadow properties, and we confront them with the EHT measurements of M87\* and Sgr A\*. We further extract independent constraints from the periastron precession of the S2 star and we examine the predictions for strong gravitational lensing using the Bozza formalism. By combining these complementary probes, we obtain robust and mutually consistent bounds on the deformation parameter  $\alpha$ , allowing us to identify which classes of  $f(Q)$  black holes remain observationally viable in the strong-gravity regime.

The remainder of this manuscript is organized as follows. Section II derives the black hole solutions and their horizon structure for the two ansätze of the affine connection. Section III analyzes the photon sphere and black hole shadow. Section IV confronts the model with EHT observations of M87\* and Sgr A\*. Section V derives constraints from the orbital dynamics of the S2 star. Section VI investigates strong gravitational lensing and provides further bounds on the model. Finally, Section VII summarizes our findings and discusses their implications.

## II. BLACK HOLE SOLUTIONS IN $f(Q)$ GRAVITY

In this section we summarize the static, spherically symmetric black-hole solutions of covariant  $f(Q)$  gravity derived in Ref. [53], which form the basis for the observational tests carried out in later sections. We begin with the action,

$$S = \frac{1}{16\pi} \int d^4x \sqrt{-g} f(Q) + S_{\text{matter}}, \quad (2.1)$$

where  $f(Q)$  is a free function of the nonmetricity scalar  $Q$ , and  $S_{\text{matter}}$  is the matter action. The latter is constructed from the nonmetricity tensor

$$Q_{\alpha\mu\nu} = \nabla_\alpha g_{\mu\nu} = \partial_\alpha g_{\mu\nu} - \Gamma_{\alpha\mu}^\lambda g_{\lambda\nu} - \Gamma_{\alpha\nu}^\lambda g_{\mu\lambda},$$

and is defined as

$$Q = -Q_{\alpha\mu\nu} P^{\alpha\mu\nu}, \quad (2.2)$$

where  $P^{\alpha}_{\mu\nu}$  is the nonmetricity conjugate,

$$P^{\alpha}_{\mu\nu} = -\frac{1}{4}Q^{\alpha}_{\mu\nu} + \frac{1}{2}Q_{(\mu}{}^{\alpha}{}_{\nu)} + \frac{1}{4}(Q^{\alpha} - \tilde{Q}^{\alpha})g_{\mu\nu} - \frac{1}{4}\delta_{(\mu}^{\alpha}Q_{\nu)}, \quad (2.3)$$

with traces  $Q_\alpha \equiv Q_{\alpha}{}^{\mu}{}_{\mu}$  and  $\tilde{Q}_\alpha \equiv Q^{\mu}{}_{\alpha\mu}$ .

Varying the action with respect to the metric and the affine connection yields the field equations,

$$\begin{aligned} \frac{2}{\sqrt{-g}}\nabla_\alpha(\sqrt{-g}f_Q P^{\alpha}_{\mu\nu}) + \frac{1}{2}g_{\mu\nu}f \\ + f_Q(P_{\mu\alpha\beta}Q^{\alpha\beta}_{\nu} - 2Q_{\alpha\beta\mu}P^{\alpha\beta}_{\nu}) + 8\pi T_{\mu\nu} = 0, \end{aligned} \quad (2.4)$$

$$\nabla_\mu \nabla_\nu (\sqrt{-g}f_Q P^{\mu\nu}_{\alpha}) = 0, \quad (2.5)$$

where  $f_Q \equiv \partial_Q f(Q)$ .

After symmetry reduction of metric and connection imposed by the torsionless and stationary condition (see the details in [90]), we obtain the following expressions

$$\begin{aligned} \partial_r g_{tt} = -\frac{g_{tt}[2f_Q + g_{rr}(Qr^2 f_Q - 2f_Q - fr^2)]}{2rf_Q} \\ + \frac{g_{tt}[r^2 - g_{rr}(\Gamma^r_{\theta\theta})^2]}{\Gamma^r_{\theta\theta} r f_Q} f_{QQ} \partial_r Q, \end{aligned} \quad (2.6)$$

$$\begin{aligned} \partial_r g_{rr} = \frac{g_{rr}[2f_Q + g_{rr}(Qr^2 f_Q - 2f_Q - fr^2)]}{2rf_Q} \\ + \frac{g_{rr}[r^2 + g_{rr}(\Gamma^r_{\theta\theta})^2 + 2r\Gamma^r_{\theta\theta}]}{\Gamma^r_{\theta\theta} r f_Q} f_{QQ} \partial_r Q, \end{aligned} \quad (2.7)$$

$$\begin{aligned} Q = -\frac{1}{r^2(\Gamma^r_{\theta\theta})^2 g_{tt} g_{rr}^2} \\ \times \left\{ \partial_r g_{tt} \Gamma^r_{\theta\theta} g_{rr} [g_{rr}(\Gamma^r_{\theta\theta})^2 + r(r + 2\Gamma^r_{\theta\theta})] \right. \\ + g_{tt} [-2g_{rr}^2(\Gamma^r_{\theta\theta})^3 \Gamma^r_{rr} - r^2 \Gamma^r_{\theta\theta} \partial_r g_{rr}] \\ + g_{tt} g_{rr} [2r^2 + 4r\Gamma^r_{\theta\theta} + 2(\Gamma^r_{\theta\theta})^2 \\ \left. + 2r^2 \Gamma^r_{\theta\theta} \Gamma^r_{rr} + (\Gamma^r_{\theta\theta})^3 \partial_r g_{rr}] \right\}, \end{aligned} \quad (2.8)$$

where  $f_{QQ} \equiv \partial_Q^2 f(Q)$ .

After imposing these symmetries [90], the only nonvanishing independent component of the connection becomes

$$\Gamma^r_{\theta\theta} = \pm \frac{r}{\sqrt{B(r)}}, \quad (2.9)$$

which obeys the differential condition

$$\partial_r \Gamma^r_{\theta\theta} = -1 - \Gamma^r_{\theta\theta} \Gamma^r_{rr}. \quad (2.10)$$

The reduced field equations for  $A(r)$ ,  $B(r)$ , and  $Q(r)$  take the form (2.6)-(2.8) (see Ref. [53] for the full derivation).

We consider a static, spherically symmetric metric,

$$ds^2 = -A(r)dt^2 + B(r)dr^2 + r^2(d\theta^2 + \sin^2\theta d\varphi^2). \quad (2.11)$$

Concerning the  $f(Q)$  form, we will consider the basic model, which is a power-law correction on top of standard general relativity, namely

$$f(Q) = Q + \alpha Q^n - 2\Lambda, \quad (2.12)$$

where  $\alpha$  controls deviations from GR and  $n = 2, 3$  are the cases of interest. Note that the first case, namely  $n = 2$ , according to Taylor expansion is a good approximation of any realistic  $f(Q)$  gravity, i.e. of any theory that is a small deviation from general relativity.

Working perturbatively in  $\alpha$ , the metric components are expanded as

$$A(r) = g_{tt}^{(0)} + \alpha g_{tt}^{(1)}, \quad B(r) = g_{rr}^{(0)} + \alpha g_{rr}^{(1)}, \quad (2.13)$$

with zeroth-order terms given by the Schwarzschild-de Sitter solution,

$$g_{tt}^{(0)} = 1 - \frac{2M}{r} - \frac{\Lambda r^2}{3}, \quad g_{rr}^{(0)} = 1 + \frac{2M}{r} + \frac{\Lambda r^2}{3}. \quad (2.14)$$

Depending on the sign choice in  $\Gamma^r_{\theta\theta}$ , two families of solutions arise.

*Case I:*  $\Gamma^r_{\theta\theta} = -r/\sqrt{B(r)}$ .

$$A(r) = 1 - \frac{2M}{r} - \frac{\Lambda}{3}r^2 - \alpha \frac{(-1)^n 2^n n M^{2n-1}}{(4n-3)r^{4n-3}}, \quad (2.15)$$

$$B(r) = 1 + \frac{2M}{r} + \frac{\Lambda}{3}r^2 + \alpha \frac{(-1)^n 2^n n M^{2n-1}}{r^{4n-3}}, \quad (2.16)$$

$$Q(r) = \frac{2M^2}{r^4} + \alpha \frac{(-1)^n 2^{n+1} n M^2}{r^{4n}}. \quad (2.17)$$

*Case II:*  $\Gamma^r_{\theta\theta} = +r/\sqrt{B(r)}$ .

$$A(r) = 1 - \frac{2M}{r} - \frac{\Lambda}{3}r^2 - \alpha \frac{2^{3n-1}}{(2n-3)r^{2n-2}}, \quad (2.18)$$

$$B(r) = 1 + \frac{2M}{r} + \frac{\Lambda}{3}r^2 + \alpha \frac{2^{3n-1}(2n^2 - 3n + 1)}{(2n-3)r^{2n-2}}, \quad (2.19)$$

$$Q(r) = \frac{8}{r^2} - \alpha \frac{2^{3n+1}(n-1)}{r^{2n}}. \quad (2.20)$$

The two branches exhibit qualitatively different radial corrections: in Case I the deviations scale as  $r^{3-4n}$ , while in Case II they scale as  $r^{2-2n}$ . This distinction will later prove crucial, as only Case II leads to deviations large enough to be constrained by current strong-field observations.

Let us proceed by determining the event horizon locations, neglecting the cosmological constant for simplicity. Imposing  $A(r_h) = 0$  we obtain polynomial equations for  $r_h$ , which can be solved perturbatively, and thus the horizon corrections can be extracted.

*Case I:*

$$r_h^{(I,n=2)} \approx 2M \left( 1 + \frac{\alpha}{20M^2} \right), \quad (2.21)$$

$$r_h^{(I,n=3)} \approx 2M \left( 1 - \frac{\alpha}{192M^4} \right). \quad (2.22)$$

*Case II:*

$$r_h^{(II,n=2)} \approx 2M \left( 1 + \frac{8\alpha}{M^2} \right), \quad (2.23)$$

$$r_h^{(II,n=3)} \approx 2M \left( 1 + \frac{16\alpha}{3M^4} \right). \quad (2.24)$$

For completeness, in Table I we list the numerical values of the event horizon location  $\alpha$  in the range  $[0, 0.5]$ , in Planck mass units. As we can see, these results demonstrate that the Case II branch exhibits much stronger deviations from the Schwarzschild radius, a feature that will be essential for deriving observational constraints in the following sections.

TABLE I: Event horizon radius  $r_h$  for the two solution branches of  $f(Q)$  gravity model with different values of  $\alpha$ , and  $M = 1$ .

$\alpha$	Event Horizon Radius $r_h$			
	Case I, $n = 2$	Case I, $n = 3$	Case II, $n = 2$	Case II, $n = 3$
0.0	2.00000	2.00000	2.00000	2.00000
0.1	2.00494	1.99895	3.04939	2.34040
0.2	2.00975	1.99790	3.72022	2.40510
0.3	2.01444	1.99683	4.25500	2.43243
0.4	2.01900	1.99576	4.71500	2.44762
0.5	2.02344	1.99467	5.12311	2.45714

Since all strong-field predictions in the following sections rely on the perturbative ansatz

$$A(r) = A_0(r) + \alpha A_1(r), \quad B(r) = B_0(r) + \alpha B_1(r), \quad (2.25)$$

it is essential to verify that the corrections proportional to  $\alpha$  remain small throughout the region where observational constraints are extracted. In the absence of such a check, one cannot guarantee that the perturbative series is under control, especially near the photon sphere where the sensitivity to deviations from GR is maximal.

A practical way to assess the validity of the expansion is to evaluate the dimensionless ratios

$$\epsilon_A(r) \equiv \left| \frac{\alpha A_1(r)}{A_0(r)} \right|, \quad \epsilon_B(r) \equiv \left| \frac{\alpha B_1(r)}{B_0(r)} \right|, \quad (2.26)$$

and demand that  $\epsilon_A(r)$  and  $\epsilon_B(r)$  remain well below unity in the domain of interest. For black-hole shadow and strong-lensing observables, the relevant scale is the photon-sphere neighborhood  $r \simeq r_c \approx 3M$ . Therefore, we evaluate  $\epsilon_A(r)$  at  $r = 3M$  for both branches.

*Case I.* For Case I, the  $\alpha$ -correction to the lapse function behaves as  $A_1(r) \propto r^{3-4n}$ . At  $r = 3M$ , this yields

$$\epsilon_A^{(I)}(3M) \simeq \left| \alpha \frac{k_n}{3^{4n-3}} \frac{1}{M^{2n-2} A_0(3M)} \right|. \quad (2.27)$$

Using  $A_0(3M) = 1 - 2/3 \simeq 1/3$ , we obtain the compact estimate

$$\epsilon_A^{(I)}(3M) \approx 3 \left| \frac{\alpha k_n}{3^{4n-3} M^{2n-2}} \right|. \quad (2.28)$$

Even for  $\alpha/M^{2n-2}$  at the upper end of the observationally allowed range,  $\epsilon_A^{(I)}(3M)$  remains  $\mathcal{O}(10^{-3})$ – $\mathcal{O}(10^{-2})$ , confirming that the perturbative treatment is self-consistent in this branch.

*Case II.* In contrast, the Case II solutions produce much larger corrections, since the  $\alpha$ -term scales as  $A_1(r) \propto r^{2-2n}$ , which decays more slowly near the photon sphere. Evaluating (2.26) at  $r = 3M$  gives

$$\epsilon_A^{(II)}(3M) \simeq 3 \left| c_n \frac{\alpha}{3^{2n-2} M^{2n-2}} \right|. \quad (2.29)$$

For  $n = 2$ , this becomes

$$\epsilon_A^{(II)}(3M) \approx \mathcal{O}(10) \times \left| \frac{\alpha}{M^2} \right|. \quad (2.30)$$

Hence, values as large as  $\alpha/M^2 \sim 10^{-1}$  would already imply  $\epsilon_A^{(II)}(3M) \gtrsim 1$ , signalling a breakdown of the perturbative expansion. This observation explains why Case II deviations grow rapidly with  $\alpha$  and why the observational constraints derived later naturally restrict  $\alpha/M^{2n-2}$  to the few-percent level or below.

The above estimates demonstrate that the perturbative series is uniformly well behaved for Case I over the entire parameter region considered. For Case II, the expansion remains valid only when the dimensionless quantity  $\alpha/M^{2n-2}$  is sufficiently small, ensuring that all phenomenological predictions presented in this work are derived within the consistent domain of the perturbative solution.

A notable feature of the covariant formulation of  $f(Q)$  gravity is that static, spherically symmetric solutions admit two distinct families determined by the sign choice in the single non-vanishing independent component of the affine connection (2.9). Although this sign appears at first sight as a mere algebraic freedom, it in fact corresponds to two physically inequivalent realizations of the compatible symmetric connection. Because the affine structure is dynamical in  $f(Q)$  gravity, the choice in Eq. (2.9) affects the form of the nonmetricity scalar, the effective gravitational potential, and ultimately the curvature felt by null and timelike geodesics. For clarity, we summarize the physical distinctions between the two branches.

Using Eq. (2.9), the nonmetricity scalar takes the schematic form

$$Q(r) \sim (\Gamma^r_{\theta\theta})^2 \times \mathcal{F}[A(r), B(r), A'(r), B'(r)], \quad (2.31)$$

therefore changing the sign of  $\Gamma^r_{\theta\theta}$  does not simply flip  $Q$ , but modifies the radial dependence of the subleading contributions entering  $\mathcal{F}$ . As a result, Case I and Case II yield distinct scaling behaviors of the  $\alpha$ -dependent corrections. The Case I branch generates rapidly decaying corrections  $\propto r^{3-4n}$ , whereas Case II produces much more slowly decaying terms  $\propto r^{2-2n}$ . This difference alone already anticipates the observational outcomes found later: Case I remains extremely close to GR,

while Case II allows sizable deviations near the photon sphere.

The sign in Eq. (2.9) is tied to how the symmetric connection accounts for the radial change of the two-sphere geometry in spacetime. In GR, the Levi-Civita connection fixes this sign uniquely via metric compatibility. In  $f(Q)$  gravity, however, the connection is independent and compatibility is replaced by a weaker condition involving the nonmetricity tensor. Thus, the two branches correspond to inequivalent ways to encode the extrinsic variation of the angular sector into the affine structure. Since nonmetricity governs how lengths and angles vary under parallel transport, the sign essentially determines the direction in which angular intervals deform as one moves radially.

The two branches lead to different radial corrections in  $A(r)$  and  $B(r)$ :

$$\text{Case I:} \quad A(r) = A_0(r) - \alpha \delta A_I(r), \quad (2.32)$$

$$\text{Case II:} \quad A(r) = A_0(r) - \alpha \delta A_{II}(r), \quad (2.33)$$

with  $\delta A_{II}(r)$  much larger than  $\delta A_I(r)$  near  $r \sim \mathcal{O}(M)$ . Operationally, this means that Case II modifies the effective gravitational potential far more strongly. This distinction becomes evident in the photon-sphere position, shadow radius, and strong-deflection coefficients computed in later sections.

Obviously, both branches satisfy the full set of field equations derived from the variational principle. Neither violates the symmetry assumptions nor introduces spurious torsion. Furthermore, both reduce smoothly to the Schwarzschild solution as  $\alpha \rightarrow 0$ , indicating that the sign choice does not produce a pathological GR limit. The difference between the branches therefore reflects the inherent flexibility of the affine structure in symmetric teleparallel gravity, where multiple connections can be compatible with the same metric while leading to physically distinct phenomenology.

Due to the fact that Case I corrections decay rapidly with radius, its deviations from GR remain unobservably small for astrophysical black holes. By contrast, Case II exhibits slowly decaying  $\alpha$ -terms that survive at the photon sphere, thereby allowing shadow distortions and strong-lensing effects within the sensitivity of current and near-future instruments. The branch structure of the theory thus naturally explains why only Case II yields phenomenology that can be meaningfully constrained with EHT, S2, and strong-field lensing observations.

In summary, the two branches correspond to physically inequivalent realisations of the symmetric connection, each leading to qualitatively different nonmetricity and strong-field behavior. This distinction underlies all observational results in the remainder of the paper and provides a clear, geometric interpretation of why only one branch develops sizable departures from the Schwarzschild geometry.

### III. BLACK HOLE SHADOWS

In this section we study null geodesics around the black hole solutions presented in Sec. II and we derive the corresponding photon-sphere and shadow radii. We restrict attention to equatorial motion ( $\theta = \pi/2$ ) in the static, spherically symmetric metric (2.11). For null geodesics ( $ds^2 = 0$ ), the timelike and rotational Killing vectors generate two conserved quantities: the energy  $E$  and angular momentum  $L$ ,

$$E = A(r) \frac{dt}{d\lambda}, \quad L = r^2 \frac{d\phi}{d\lambda}, \quad (3.1)$$

where  $\lambda$  is an affine parameter. Hence,

$$\frac{dt}{d\lambda} = \frac{E}{A(r)}, \quad \frac{d\phi}{d\lambda} = \frac{L}{r^2}. \quad (3.2)$$

Imposing the null condition  $g_{\mu\nu} \dot{x}^\mu \dot{x}^\nu = 0$  gives

$$-A(r) \left( \frac{dt}{d\lambda} \right)^2 + B(r) \left( \frac{dr}{d\lambda} \right)^2 + r^2 \left( \frac{d\phi}{d\lambda} \right)^2 = 0, \quad (3.3)$$

which, after substituting the above relations, becomes

$$B(r) \left( \frac{dr}{d\lambda} \right)^2 + \frac{L^2}{r^2} = \frac{E^2}{A(r)}. \quad (3.4)$$

Introducing the impact parameter  $b \equiv L/E$  and using  $dr/d\lambda = (dr/d\phi)(d\phi/d\lambda) = (dr/d\phi)L/r^2$ , we obtain

$$\frac{B(r)}{r^4} \left( \frac{dr}{d\phi} \right)^2 + \frac{1}{r^2} = \frac{1}{b^2 A(r)}. \quad (3.5)$$

It is convenient to work with the inverse radial coordinate  $u \equiv 1/r$ . Noting that  $dr/d\phi = -u^{-2} du/d\phi$ , we rewrite Eq. (3.5) as

$$\left( \frac{du}{d\phi} \right)^2 = \frac{1}{B(u)} \left[ \frac{1}{b^2 A(u)} - u^2 \right], \quad (3.6)$$

which is the orbit equation for null geodesics. A circular photon orbit (the photon sphere) at radius  $r_c$  (or  $u_c = 1/r_c$ ) is characterized by

$$\left. \frac{du}{d\phi} \right|_{u_c} = 0, \quad \left. \frac{d^2 u}{d\phi^2} \right|_{u_c} = 0. \quad (3.7)$$

The first condition implies, from Eq. (3.6),

$$\frac{1}{b^2 A(u_c)} - u_c^2 = 0 \quad \Rightarrow \quad b^2 = \frac{1}{u_c^2 A(u_c)} = \frac{r_c^2}{A(r_c)}, \quad (3.8)$$

so that the critical impact parameter is

$$b_c = \frac{r_c}{\sqrt{A(r_c)}}. \quad (3.9)$$

For an observer at infinity,  $b_c$  is precisely the shadow radius  $R_s$ .

The second condition,  $d^2 u/d\phi^2 = 0$ , yields the photon-sphere equation. Taking the derivative of Eq. (3.6) with respect to  $\phi$  gives

$$2 \frac{du}{d\phi} \frac{d^2 u}{d\phi^2} = \frac{d}{d\phi} \left\{ \frac{1}{B(u)} \left[ \frac{1}{b^2 A(u)} - u^2 \right] \right\}. \quad (3.10)$$

At  $u = u_c$  we have  $du/d\phi = 0$ , hence the right-hand side must vanish, which leads (after some algebra) to

$$\left. \frac{d}{du} \left( \frac{1}{A(u)u^2} \right) \right|_{u_c} = 0. \quad (3.11)$$

In terms of the radial coordinate this is equivalent to

$$\left. \frac{d}{dr} \left( \frac{A(r)}{r^2} \right) \right|_{r_c} = 0 \quad \Rightarrow \quad \frac{A'(r_c)}{A(r_c)} = \frac{2}{r_c}, \quad (3.12)$$

which determines the photon-sphere radius  $r_c$ . As is evident from Eqs. (3.9) and (3.12), the lapse function  $B(r)$  does not affect the shadow radius seen by a distant observer.

Thus, to compute the shadow radius for the black hole solutions of Sec. II, we first solve Eq. (3.12) perturbatively for  $r_c$  and then we substitute the result into Eq. (3.9), obtaining the  $\alpha$ -dependent corrections to  $R_s$ .

**Case I.** For the Case I branch we define

$$k_n = \frac{(-1)^n 2^n n}{4n - 3}, \quad p_n = (-1)^n 2^n n, \quad (3.13)$$

so that

$$A(r) = 1 - \frac{2M}{r} - \alpha k_n \frac{M^{2n-1}}{r^{4n-3}}, \quad (3.14)$$

$$A'(r) = \frac{2M}{r^2} + \alpha k_n (4n - 3) \frac{M^{2n-1}}{r^{4n-2}}. \quad (3.15)$$

Introducing the function

$$F(r) \equiv r A'(r) - 2A(r), \quad (3.16)$$

the photon-sphere condition (3.12) is equivalent to  $F(r_c) = 0$ , with

$$F(r) = \frac{6M}{r} + \alpha k_n (4n - 1) \frac{M^{2n-1}}{r^{4n-3}} - 2. \quad (3.17)$$

For  $n = 2$  this reduces to

$$6Mr_c^4 - 2r_c^5 + \alpha \frac{28}{5} M^3 = 0. \quad (3.18)$$

Setting  $r_c = 3M + \epsilon$  and expanding to first order in  $\epsilon$  (for small  $\alpha$ ) yields

$$\epsilon = \frac{14\alpha}{405M} \approx 0.034568 \frac{\alpha}{M}, \quad (3.19)$$

and thus

$$r_c^{(I, n=2)} \approx 3M + 0.03457 \frac{\alpha}{M}. \quad (3.20)$$



Substituting this into Eq. (3.9), the corresponding shadow radius becomes

$$R_s^{(I,n=2)} \approx 3\sqrt{3} M \left(1 + 0.00494 \frac{\alpha}{M^2}\right). \quad (3.21)$$

Repeating the same procedure for  $n = 3$  we obtain

$$r_c^{(I,n=3)} \approx 3M - 0.002236 \frac{\alpha}{M^3}, \quad (3.22)$$

and

$$R_s^{(I,n=3)} \approx 3\sqrt{3} M \left(1 - 0.000203 \frac{\alpha}{M^4}\right). \quad (3.23)$$

**Case II.** For the Case II branch, the photon-sphere equation simplifies considerably. For  $n = 2$  one finds

$$F(r) = r^2 - 3Mr - 64\alpha, \quad (3.24)$$

and imposing  $F(r_c) = 0$  yields, to first order in  $\alpha$ ,

$$r_c^{(II,n=2)} \approx 3M + 21.333 \frac{\alpha}{M}, \quad (3.25)$$

with shadow radius

$$R_s^{(II,n=2)} \approx 5.19615 M \left(1 + 5.333 \frac{\alpha}{M^2}\right). \quad (3.26)$$

For  $n = 3$  we obtain

$$r_c^{(II,n=3)} \approx 3M - 1.8963 \frac{\alpha}{M^3}, \quad (3.27)$$

and

$$R_s^{(II,n=3)} \approx 3\sqrt{3} M \left(1 + 1.580 \frac{\alpha}{M^4}\right). \quad (3.28)$$

These expressions show that, while the Case I corrections to the shadow radius are relatively small, the Case II branch can lead to significantly larger deviations from the GR value, especially for  $n = 2$ . This will make Case II the primary target of the observational constraints derived from EHT, S2-star dynamics, and strong lensing in the following sections.

TABLE II: Photon sphere radius  $r_c$  and shadow radius  $R_s$  for the two solution branches of covariant  $f(Q)$  gravity. The dimensions of the parameter  $\alpha$  are: for  $n = 2$ ,  $[\alpha] = M^2$ ; for  $n = 3$ ,  $[\alpha] = M^4$ , where  $M$  is the BH mass.

Case	$n$	$r_c$ (photon sphere)	$R_s$ (shadow radius)
I	2	$3M + 0.03457 \frac{\alpha}{M}$	$3\sqrt{3}M \left(1 + 0.00494 \frac{\alpha}{M^2}\right)$
I	3	$3M - 0.002236 \frac{\alpha}{M^3}$	$3\sqrt{3}M \left(1 - 0.000203 \frac{\alpha}{M^4}\right)$
II	2	$3M + 21.333 \frac{\alpha}{M}$	$3\sqrt{3}M \left(1 + 5.333 \frac{\alpha}{M^2}\right)$
II	3	$3M - 1.8963 \frac{\alpha}{M^3}$	$3\sqrt{3}M \left(1 + 1.580 \frac{\alpha}{M^4}\right)$

In Table II we present an overview of the shadow and photon-sphere results. Since the deviation parameter  $\alpha$  is assumed to be small, we compute the photon-sphere radius  $r_c$  and the shadow radius  $R_s$  numerically

for  $\alpha \in [0, 0.5]$ , with the results displayed in Table III. As the Tables show, the Case I branch remains practically indistinguishable from the GR prediction, with corrections well below current observational sensitivity. In contrast, the Case II branch exhibits clear and monotonic deviations from GR: increasing  $\alpha$  leads to a larger shadow size, making these solutions observationally testable with horizon-scale imaging.

TABLE III: Photon sphere radius  $r_c$  and shadow radius  $R_s$  for the two solution branches of covariant  $f(Q)$  gravity, with different values of  $\alpha$ , and  $M = 1$ .

$\alpha$	Case I, $n = 2$	Case I, $n = 3$	Case II, $n = 2$	Case II, $n = 3$
	$r_c$	$R_s$	$r_c$	$R_s$
0.0	3.0000	5.1962	3.0000	5.1962
0.1	3.0035	5.1987	2.9998	5.1960
0.2	3.0069	5.2013	2.9996	5.1959
0.3	3.0104	5.2039	2.9993	5.1958
0.4	3.0138	5.2064	2.9991	5.1957
0.5	3.0173	5.2090	2.9989	5.1956

Fig. 1 illustrates the corresponding shadow profiles for the Case II family with  $n = 2$  and  $n = 3$ , where we can observe the significant dependence of the shadow radius on the deformation parameter. To visualize photon trajectories, Fig. 2 shows sample equatorial null geodesics for the representative case  $n = 2$  and  $\alpha = 0.1$ . Photons with impact parameter  $b < b_c \simeq 6.9$  are captured by the black hole, while those with  $b > b_c$  escape to infinity, thus forming the boundary of the observable shadow.

Before turning to observational tests, it is helpful to provide an intuitive explanation of how nonmetricity alters the propagation of light in covariant  $f(Q)$  gravity. Although the technical derivation in the previous parts follows directly from the modified field equations, the underlying physical picture can be summarized in a simple way.

In general relativity, the Levi-Civita connection preserves both lengths and angles during parallel transport. In symmetric teleparallel gravity, the connection is torsionless and curvature-free, but it does not preserve the metric. The nonmetricity tensor  $Q_{\alpha\mu\nu} = \nabla_\alpha g_{\mu\nu}$  measures precisely how lengths and angles change when transported across spacetime. This change is usually negligible far from compact objects, however it becomes amplified in strong fields, where the geometry varies rapidly.

In  $f(Q)$  gravity the geodesics of photons remain the extremals of the metric, not of the affine connection. However, the metric is no longer governed solely by Einstein's equations, and its radial profile is affected by the nonmetricity scalar  $Q$ . The result is that null geodesics, although defined in the usual way by  $ds^2 = 0$ , respond to a spacetime geometry whose shape has been distorted by the nonmetricity-driven corrections. That is why the effect is conceptually distinct from modified-optics or birefringent theories: the photons behave normally, but the stage on which they move has been subtly reshaped.

The practical consequence of this geometric reshaping

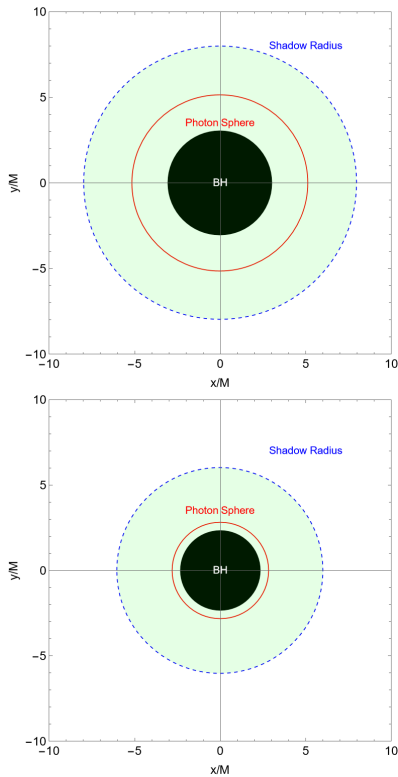


FIG. 1: The black hole shadow of Case II solution in the equatorial plane with  $n = 2$  (upper panel), and  $n = 3$  (lower panel) for fixed value of  $\alpha = 0.1$  in Planck mass units.

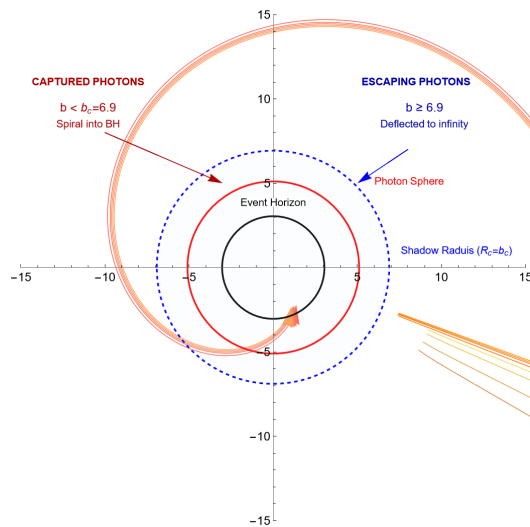


FIG. 2: A representative example of null geodesics in the equatorial plane of the Case II black-hole solution with  $n = 2$  and  $\alpha = 0.1$  in Planck mass units.

can be seen more easily near the photon sphere. A small deviation in the metric component  $A(r)$  near  $r \simeq 3M$  can shift the condition (3.12) which determines the radius of the unstable circular orbit of photons. Since the non-metricity corrections in the Case II branch decay slowly

with radius, they remain relevant at the photon sphere and can either strengthen or weaken the effective gravitational potential felt by null rays. In turn, this shifts both the location of the light ring and the apparent size of the shadow.

Light rays that just graze the photon sphere are exponentially sensitive to the shape of the effective potential. A small nonmetricity-induced deformation of  $A(r)$  therefore produces compensated changes in the critical impact parameter  $b_c$ , the size and displacement of the shadow boundary, the strong-deflection coefficients  $\bar{a}$  and  $\bar{b}$ , and the separation of relativistic images in strong lensing.

The slow decrease of the Case II corrections implies that these effects survive into the regime probed by the Event Horizon Telescope, while the more rapidly decaying Case I corrections become effectively invisible at astrophysical scales. In summary, nonmetricity modifies the background geometry rather than the photon propagation rule itself. This subtle but important distinction explains why  $f(Q)$  gravity predicts distinctive signatures in light deflection and black-hole shadow observables while remaining compatible with the geometric-optics limit of photon transport.

#### IV. CONSTRAINTS FROM EVENT HORIZON TELESCOPE OBSERVATIONS

The strong-field signatures of black hole spacetimes offer a powerful probe of modified gravity theories. Among these, the Event Horizon Telescope (EHT) observations of the supermassive black holes M87\* [56, 57] and Sgr A\* [58] provide the most precise horizon-scale measurements to date. The EHT effectively resolves the lensed photon orbit surrounding the event horizon, allowing the extraction of an angular diameter associated with the shadow, a quantity that depends solely on the near-horizon geometry, and therefore offers a direct test of the metric. In this section we use the EHT shadow measurements to place observational constraints on the deformation parameter  $\alpha$  appearing in Case II black-hole solutions of  $f(Q)$  gravity.

The EHT is a global very-long-baseline interferometer (VLBI) operating at 230 GHz, achieving an angular resolution of order  $\sim 20 \mu\text{as}$ . At this wavelength, the emission surrounding the black hole becomes optically thin, and the interferometric baselines are long enough to reconstruct the brightness distribution near the photon ring. The observable extracted by the EHT collaboration is an intensity-weighted ring diameter, which closely tracks the theoretical shadow radius  $R_s$  for any metric whose near-horizon structure is approximately circular and stationary.

While numerical radiative-transfer models contribute to the detailed interpretation of the images, several studies [91, 92] have shown that the inferred shadow diameter can be treated with minimal model dependence. This allows for a direct comparison between the theoretical

shadow radius of a given black hole solution and the observationally inferred values. In particular, one can express the measured angular shadow diameter  $\theta_{\text{sh}}$  as

$$\theta_{\text{sh}} = \frac{2R_s}{D}, \quad (4.1)$$

where  $R_s$  is the theoretical shadow radius in units of mass  $M$ , and  $D$  is the distance to the source. Given independent estimates of  $D$  and  $M$ , the EHT data thereby place constraints on any theory that modifies  $R_s$  relative to its GR value  $R_s^{\text{GR}} = 3\sqrt{3}M$ .

As demonstrated in Fig. 1 and in Table III, the Case II solutions exhibit a substantially stronger dependence on the deformation parameter  $\alpha$  than the Case I solutions. This is a direct consequence of the different radial scaling of the  $\alpha$ -corrections in the two families of solutions: Case II introduces corrections of order  $\sim r^{2-2n}$ , which decay more slowly than the  $\sim r^{3-4n}$  corrections of Case I, and therefore remain non-negligible near the photon sphere ( $r_c \simeq 3M$ ). This enhanced sensitivity makes Case II a natural target for observational constraints.

For definiteness, we summarise the leading corrections:

$$R_s^{(\text{II})}(n=2) \approx 3\sqrt{3}M \left(1 + 5.333 \frac{\alpha}{M^2}\right), \quad (4.2)$$

$$R_s^{(\text{II})}(n=3) \approx 3\sqrt{3}M \left(1 + 1.580 \frac{\alpha}{M^4}\right). \quad (4.3)$$

These expressions show that even for  $\alpha \sim 10^{-2}M^2$ – $10^{-1}M^2$ , the shift in  $R_s$  can reach several percent, which is within the sensitivity of current EHT measurements. This motivates confronting the model with observations.

#### A. Constraints from the M87\* shadow

For M87\*, the EHT reports an angular ring diameter of  $\theta_{\text{ring}} \approx 42 \pm 3 \mu\text{as}$ , corresponding to a dimensionless shadow size of

$$\frac{2R_s}{M} \approx 11.0 \pm 1.5, \quad (4.4)$$

after combining the angular size with the distance [91].

Using the modified shadow radii of the Case II black hole, we compare the predicted shadow diameter with the allowed observational band. The results, illustrated in Fig. 3, show that the model remains compatible with the EHT measurement provided the deformation parameter satisfies

$$0 < \frac{\alpha}{M^2} < 0.047 \quad (n=2), \quad (4.5)$$

$$0 < \frac{\alpha}{M^4} < 0.27 \quad (n=3). \quad (4.6)$$

Larger values of  $\alpha$  would increase the shadow radius beyond the upper observational bound, thereby being ruled out. The constraints are therefore primarily upper bounds, with M87\* providing the most stringent restrictions for  $n=2$ .

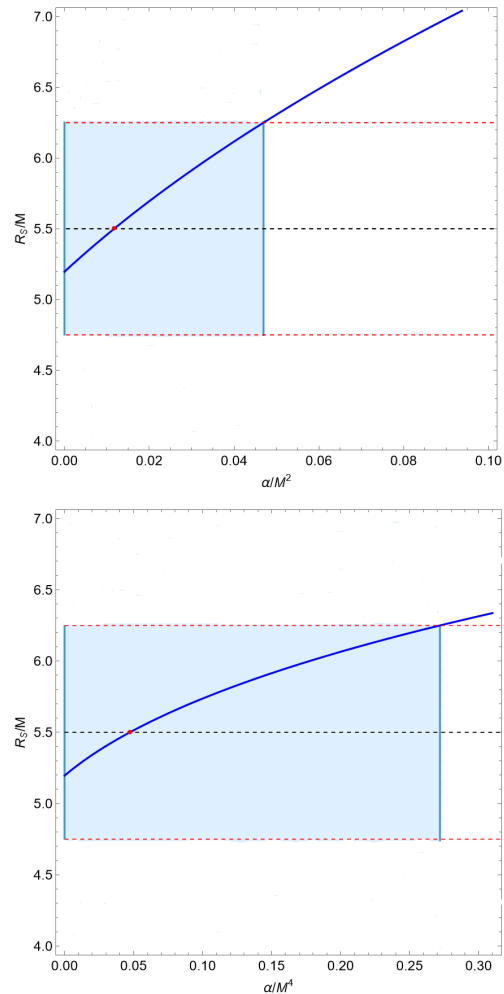


FIG. 3: The allowed range of  $\alpha/M^2$  (upper panel), and  $\alpha/M^4$  (lower panel) for Case II black-hole solution with  $n=2, 3$  in light of EHT diameter measurement of M87\*. The black-dashed line represents the central value of  $R_s/M$  in EHT data, while the red-dashed lines mark the lower and upper permissible bounds.

#### B. Constraints from the Sgr A\* shadow

The case of Sgr A\* is more challenging due to variability and scattering effects, but using the mass-to-distance ratio inferred from Keck and VLTI measurements, Ref. [92] reports a  $2\sigma$  interval:

$$4.21 \lesssim \frac{R_s}{M} \lesssim 5.56. \quad (4.7)$$

This bound can similarly be used to constrain the shift in the shadow radius induced by  $\alpha$ . Substituting the theoretical expressions for  $R_s^{(\text{II})}$  into this interval yields an independent and complementary constraint on  $\alpha$ , illustrated in Fig. 4. Although the Sgr A\* bounds are generally weaker than those from M87\*, they remain consistent with the same allowed intervals and exclude significantly larger deviations from GR.



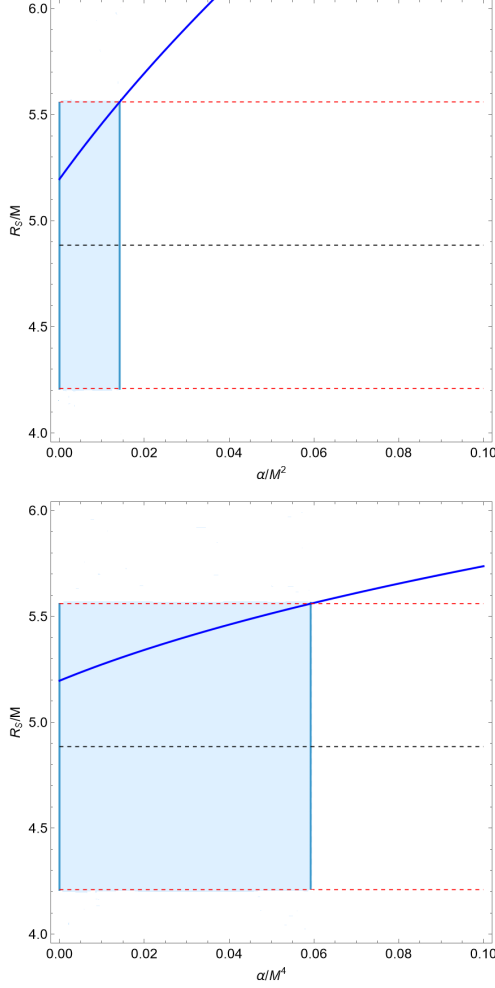


FIG. 4: The allowed range of  $\alpha/M^2$  (upper panel), and  $\alpha/M^4$  (lower panel) for Case II black-hole solution with  $n = 2, 3$  in light of EHT diameter measurement of Sgr A\*. The black-dashed line represents the central value of  $R_s/M$  in EHT data, while the red-dashed lines mark the lower and upper permissible bounds.

### C. Summary of EHT constraints

Taken together, the M87\* and Sgr A\* observations place robust constraints on the deformation parameter of the Case II covariant  $f(Q)$  black hole. The bounds obtained from M87\*, owing to its larger mass and better-defined image structure, are the most stringent, bounding the fractional corrections of order  $\alpha/M^2$  to below a few percent in the  $n = 2$  case, and placing meaningful constraints on  $\alpha/M^4$  for  $n = 3$ . These results demonstrate that the current EHT data already probe nonmetricity-induced deviations from GR at the horizon scale, and thus future higher-resolution observations will further tighten these limits.

## V. CONSTRAINTS FROM S2 STAR PRECESSION

The stellar dynamics of the Galactic Center provide one of the cleanest tests of gravity in the weak-to-intermediate field regime surrounding a supermassive black hole. Among the stars orbiting Sgr A\*, the S2 star (also known as S0-2) plays a central role. It is a bright, massive B-type star with a short orbital period ( $\sim 16$  yr) and an exceptionally small pericenter distance ( $\sim 120$  AU). Its highly eccentric orbit, combined with precise astrometric and spectroscopic measurements from GRAVITY Keck+VLTI [94], makes S2 an outstanding natural probe of deviations from the Schwarzschild geometry of Sgr A\*.

In Newtonian gravity, the orbit of a test mass is a closed ellipse, while in GR, the curvature of spacetime induces a forward rotation of the orbit, leading to a shift in the periastron after each revolution. This periastron precession is one of the classical relativistic tests and is directly sensitive to the underlying spacetime metric. Hence, any modification to GR, such as the  $\alpha$ -dependent corrections predicted by covariant  $f(Q)$  gravity, modifies the precession rate.

In this section we use the observational measurements of S2's periastron precession to derive upper bounds on the deformation parameter  $\alpha$  for both Case I and Case II black hole geometries. The modified precession expressions based on the solutions of Ref. [53] are

$$\Delta\phi_{n=2}^I \approx \frac{6\pi M}{a(1-e^2)} + \frac{\pi\Lambda a^3(1-e^2)^3}{M} + \alpha \left[ \frac{16\pi M^2}{a^4(1-e^2)^4} + \frac{40\pi M^3}{a^5(1-e^2)^5} \right], \quad (5.1)$$

$$\Delta\phi_{n=3}^I \approx \frac{6\pi M}{a(1-e^2)} + \frac{\pi\Lambda a^3(1-e^2)^3}{M} - \alpha \left[ \frac{96\pi M^4}{a^8(1-e^2)^8} + \frac{168\pi M^5}{a^9(1-e^2)^9} \right], \quad (5.2)$$

$$\Delta\phi_{n=2}^{II} \approx \frac{6\pi M}{a(1-e^2)} + \frac{\pi\Lambda a^3(1-e^2)^3}{M} + \alpha \left[ \frac{32\pi}{a(1-e^2)M} + \frac{256\pi}{a^2(1-e^2)^2} \right], \quad (5.3)$$

$$\Delta\phi_{n=3}^{II} \approx \frac{6\pi M}{a(1-e^2)} + \frac{\pi\Lambda a^3(1-e^2)^3}{M} + \alpha \left[ \frac{512\pi}{a^3(1-e^2)^3M} + \frac{2048\pi}{a^4(1-e^2)^4} \right]. \quad (5.4)$$

The first term in each line is the standard Schwarzschild prediction, while terms proportional to  $\alpha$  encode deviations arising from the covariant  $f(Q)$  model. On Galactic scales, the cosmological constant term is negligible and as mentioned above it is omitted in our analysis.

To constrain  $\alpha$ , we compare the theoretical prediction

$$\Delta\phi_{f(Q)} = \Delta\phi_{\text{GR}} + \delta\phi_{f(Q)}(\alpha), \quad (5.5)$$

with the observational result

$$\Delta\phi_{\text{obs}} = \Delta\phi_{\text{GR}} + \delta\phi_{\text{obs}}, \quad (5.6)$$

where  $\delta\phi_{\text{obs}}$  quantifies observational uncertainties or any potential deviation from GR. Requiring consistency between theory and observation imposes

$$|\delta\phi_{f(Q)}(\alpha)| \lesssim |\delta\phi_{\text{obs}}|. \quad (5.7)$$

We adopt the following observationally inferred parameters:

- Mass of Sgr A\*:  $M = 4.261 \times 10^6 M_\odot$ , corresponding to  $M \approx 6.29 \times 10^6$  km in geometric units.
- Semi-major axis: using Keck + VLTI distance  $R_0 = 8.275$  kpc, the observed angular size  $a = 0.125''$  gives  $a \approx 1.54 \times 10^{14}$  km.
- Orbital eccentricity:  $e \approx 0.884$ .
- Observed precession uncertainty: GRAVITY finds consistency with GR at the  $\sim 10\%$  level, yielding  $\delta\phi_{\text{obs}} \approx 3.52 \times 10^{-7}$  rad/orbit.

Moreover, we define

$$u = \frac{1}{a(1-e^2)}, \quad (5.8)$$

which for S2 evaluates to  $u \approx 2.97 \times 10^{-14} \text{ km}^{-1}$ . This quantity conveniently packages the strong dependence of the precession on the orbital size and eccentricity.

We proceed by inserting S2's orbital parameters into the  $\alpha$ -dependent contributions to the precession, and we impose the bound (5.7).

*Case I with  $n = 2$ .* From Eq. (6.9) we find

$$\delta\phi_{f(Q)}^{I,n=2} \approx \alpha [16\pi M^2 u^4 + 40\pi M^3 u^5].$$

The second term is suppressed by seven orders of magnitude and can be neglected. Numerically,

$$|\delta\phi_{f(Q)}^{I,n=2}| \approx |\alpha| \cdot 1.55 \times 10^{-40},$$

leading to

$$|\alpha| \lesssim 2.27 \times 10^{33} \text{ km}^2.$$

*Case I with  $n = 3$ .* From Eq. (6.10) we have

$$\delta\phi_{f(Q)}^{I,n=3} \approx -\alpha [96\pi M^4 u^8],$$

with the subleading term again negligible. We obtain

$$|\delta\phi_{f(Q)}^{I,n=3}| \approx |\alpha| \cdot 2.11 \times 10^{-80},$$

and therefore

$$|\alpha| \lesssim 1.67 \times 10^{73} \text{ km}^4.$$

*Case II with  $n = 2$ .* From Eq. (6.11) we have

$$\delta\phi_{f(Q)}^{II,n=2} \approx \alpha \left[ 32\pi \frac{u}{M} \right],$$

where the second term is negligible. Numerically we find

$$|\delta\phi_{f(Q)}^{II,n=2}| \approx |\alpha| \cdot 4.74 \times 10^{-19},$$

yielding a much tighter bound:

$$|\alpha| \lesssim 7.42 \times 10^{11} \text{ km}^2.$$

*Case II with  $n = 3$ .* From Eq. (6.12) we find

$$\delta\phi_{f(Q)}^{II,n=3} \approx \alpha \left[ 512\pi \frac{u^3}{M} \right],$$

leading to

$$|\delta\phi_{f(Q)}^{II,n=3}| \approx |\alpha| \cdot 6.71 \times 10^{-45},$$

and therefore

$$|\alpha| \lesssim 5.25 \times 10^{37} \text{ km}^4.$$

TABLE IV: Constraints on  $\alpha$ -parameter from S2 star precession data.

Case	$n$	Dimensional Bound	Dimensionless Bound
I	2	$ \alpha  \lesssim 10^{33} \text{ km}^2$	$\frac{ \alpha }{M^2} \lesssim 10^{20}$
I	3	$ \alpha  \lesssim 10^{73} \text{ km}^4$	$\frac{ \alpha }{M^4} \lesssim 10^{46}$
II	2	$ \alpha  \lesssim 10^{12} \text{ km}^2$	$\frac{ \alpha }{M^2} \lesssim 10^{-2}$
II	3	$ \alpha  \lesssim 10^{38} \text{ km}^4$	$\frac{ \alpha }{M^4} \lesssim 10^{10}$

In summary, as we see, the S2 constraints are naturally much weaker than those derived from the EHT shadow measurements, since the S2 orbit probes the spacetime at scales  $r \sim 10^{13}\text{--}10^{14}$  km, far beyond the photon sphere. Nevertheless, they provide a valuable complementary test in a different dynamical regime and are fully consistent with the bounds obtained from M87\* and Sgr A\* imaging. Expressing the constraints in dimensionless combinations such as  $\alpha/M^2$  or  $\alpha/M^4$  enhances their interpretability. Table IV summarizes the complete set of bounds.

## VI. STRONG LENSING CONSTRAINTS

Gravitational lensing in the strong-field regime provides a powerful and highly sensitive probe of the spacetime geometry near compact objects, making it an excellent observational test for modified gravity theories. In the context of covariant  $f(Q)$  gravity, deviations from

GR modify both the location of the photon sphere and the behavior of light deflection near it, leading to potentially observable signatures. In this section we review the strong-deflection formalism and we apply it to the black-hole solutions obtained above, in order to quantify their impact on lensing observables and derive constraints on the parameter  $\alpha$ .

### A. Strong-field deflection angle and Bozza formalism

The theoretical framework for strong-field gravitational lensing was established through a series of key developments. The pioneering work of Virbhadra and Ellis (VE) [95] shifted the focus from weak-field deflections to the strong-field regime by numerically showing that light rays performing multiple loops around a compact object generate an infinite sequence of relativistic images. Subsequently, Frittelli, Kling, and Newman (FKN) [96] placed the subject on a rigorous mathematical footing by formulating lensing observables directly from the geometry of the observer's past light cone, without invoking weak-field approximations. Building on these advances, Bozza [97] derived a universal analytic expression for the deflection angle in the strong-field limit. By carefully expanding the deflection integral near the photon sphere, he demonstrated that its divergence is logarithmic and universal, thereby providing a practical and powerful method to compute lensing observables for any spherically symmetric spacetime that possesses a photon sphere.

In particular, in Ref. [95], it was shown that for a static, spherically symmetric metric of the form

$$ds^2 = -A(r) dt^2 + B(r) dr^2 + C(r) (d\theta^2 + \sin^2 \theta d\phi^2), \quad (6.1)$$

the deflection angle  $\hat{\beta}(r_0)$  of a light ray with closest approach radius  $r_0$  is

$$\hat{\beta}(r_0) = -\pi + 2 \int_{r_0}^{\infty} \frac{dr}{\sqrt{\frac{C(r)}{B(r)} \sqrt{\frac{A(r_0)C(r)}{A(r)C(r_0)} - 1}}}. \quad (6.2)$$

In the strong deflection limit  $r_0 \rightarrow r_c^+$ , where  $r_c$  is the photon sphere radius, this integral diverges logarithmically.

A more explicit and widely used derivation of the logarithmic expansion was obtained by Bozza [97], whose formalism has become the standard reference for strong-field lensing calculations. For the metric (6.1), the deflection angle for impact parameters  $b$  close to the critical value  $b_c$  can be written as

$$\beta_{\text{def}}(b) = -\bar{a} \ln\left(\frac{b}{b_c} - 1\right) + \bar{b} + \mathcal{O}(b - b_c), \quad (6.3)$$

where  $\bar{a}$  and  $\bar{b}$  are the strong-deflection coefficients, and  $r_c$  and  $b_c$  are the photon sphere radius and the corresponding critical impact parameter, respectively.

In order to compute  $\bar{a}$  and  $\bar{b}$ , one introduces the function

$$R(r, r_0) = \sqrt{\frac{C(r)B(r)}{C(r_0)B(r_0)}} \left( \frac{A(r_0)}{A(r)} - \frac{C(r_0)}{C(r)} \right), \quad (6.4)$$

and therefore [97]

$$\bar{a} = \sqrt{\frac{2A(r_c)C(r_c)}{C''(r_c)A(r_c) - A''(r_c)C(r_c)}}, \quad (6.5)$$

$$\bar{b} = -\pi + b_R + \bar{a} \ln\left(\frac{2C(r_c)^2 A'(r_c)^2}{A(r_c)^3 C(r_c) [C(r_c) A''(r_c) - A(r_c) C''(r_c)]}\right), \quad (6.6)$$

where the regular part  $b_R$  is given by

$$b_R = 2\bar{a} \int_0^1 \left[ \frac{1}{\sqrt{R(z, r_c) f(z)}} - \frac{1}{\bar{a}z} \right] dz, \quad (6.7)$$

with the change of variable  $z = 1 - r_c/r$  and

$$f(z) = \frac{1 - A(r_c)/A(r)}{C(r_c)/C(r) - A(r_c)/A(r)}. \quad (6.8)$$

Two remarks are worth noting here. Firstly, the coefficient  $\bar{a}$  controls the strength of the logarithmic divergence as  $b \rightarrow b_c^+$ , and for the Schwarzschild black hole, one finds  $\bar{a} = 1$ . Secondly, the coefficient  $\bar{b}$  encodes the finite offset of the deflection angle, and for Schwarzschild solution we have  $\bar{b} = \ln[216(7 - 4\sqrt{3})] - \pi \approx -0.4002$ .

Using (6.5), (6.6), and (6.3), for the Case I black hole solutions discussed in Sec. II we obtain the following  $\alpha$ -corrected expressions:

*Case I with  $n = 2$ .*

$$\begin{aligned} \bar{a} &\approx 1 - 0.07243 \frac{\alpha}{M^2}, \\ \bar{b} &\approx -0.40023 + 0.152 \frac{\alpha}{M^2}, \\ \hat{\beta}_{\text{def}}(b) &\approx -\left(1 - 0.07243 \frac{\alpha}{M^2}\right) \ln\left(\frac{b}{b_c} - 1\right) \\ &\quad - 0.40023 + 0.152 \frac{\alpha}{M^2}. \end{aligned} \quad (6.9)$$

*Case I with  $n = 3$ .*

$$\begin{aligned} \bar{a} &\approx 1 + 0.00176 \frac{\alpha}{M^4}, \\ \bar{b} &\approx -0.40023 - 0.00342 \frac{\alpha}{M^4}, \\ \hat{\beta}_{\text{def}}(b) &\approx -\left(1 + 0.00176 \frac{\alpha}{M^4}\right) \ln\left(\frac{b}{b_c} - 1\right) \\ &\quad - 0.40023 - 0.00342 \frac{\alpha}{M^4}. \end{aligned} \quad (6.10)$$

As we can see, for Case I with  $n = 2$ , the  $\alpha$ -correction appears at order  $1/M^2$ , making it in principle more relevant for stellar-mass black holes than for supermassive

ones. A positive  $\alpha$  slightly reduces  $\bar{a}$  (weaker divergence) and increases  $\bar{b}$  (larger offset), leading to small but well-defined shifts in the positions and magnifications of relativistic images. For  $n = 3$ , the corrections are suppressed by  $1/M^4$  and become effectively negligible for astrophysical black holes, rendering this case extremely close to the Schwarzschild limit.

Performing the same analysis for the Case II black hole solutions yields:

*Case II with  $n = 2$ .*

$$\begin{aligned}\bar{a} &\approx 1 - 9.244 \frac{\alpha}{M^2}, \\ \bar{b} &\approx -0.40023 + 18.5 \frac{\alpha}{M^2}, \\ \hat{\beta}_{\text{def}}(b) &\approx - \left(1 - 9.244 \frac{\alpha}{M^2}\right) \ln\left(\frac{b}{b_c} - 1\right) \\ &\quad - 0.40023 + 18.5 \frac{\alpha}{M^2}.\end{aligned}\quad (6.11)$$

*Case II with  $n = 3$ .*

$$\begin{aligned}\bar{a} &\approx 1 - 0.842 \frac{\alpha}{M^4}, \\ \bar{b} &\approx -0.40023 + 1.523 \frac{\alpha}{M^4}, \\ \hat{\beta}_{\text{def}}(b) &\approx - \left(1 - 0.842 \frac{\alpha}{M^4}\right) \ln\left(\frac{b}{b_c} - 1\right) \\ &\quad - 0.40023 + 1.523 \frac{\alpha}{M^4}.\end{aligned}\quad (6.12)$$

As we see, for the same value of  $n$ , Case II exhibits much larger corrections than Case I, reflecting the different radial dependence of the corresponding metric functions. In particular, the  $n = 2$  Case II solution shows pronounced deviations: a positive  $\alpha$  substantially decreases  $\bar{a}$  (weaker divergence) and strongly enhances  $\bar{b}$  (larger offset), with corrections roughly two orders of magnitude larger than in Case I,  $n = 2$ . The  $n = 3$  Case II corrections are smaller than in the  $n = 2$  case, but they remain significantly larger than their Case I counterparts.

In summary, these strong-lensing results indicate that Case II solutions in covariant  $f(Q)$  gravity, especially for  $n = 2$ , can lead to observationally relevant modifications in the strong deflection regime. Through their impact on the strong-deflection coefficients  $\bar{a}$  and  $\bar{b}$ , they alter the positions, separations, and magnifications of relativistic images, making these models promising targets for future high-resolution observations of black hole shadows and strong-field lensing with next-generation instruments building upon the Event Horizon Telescope.

## B. Shedding light on relativistic images with EHT data

In the strong-deflection regime, the deflection angle is fundamentally a function of the impact parameter  $b$ , as

given in (6.3). For a distant observer located at a distance  $D_{OL}$  from the black hole, the impact parameter is related to the observed angular position  $\theta$  through the standard small-angle relation

$$b = \theta D_{OL}, \quad (6.13)$$

which follows from geometric optics and the fact that the angular size of a supermassive black hole is of the order of tens of microarcseconds. Substituting (6.13) into the strong-deflection formula (6.3) gives

$$\beta(\theta) = -\bar{a} \ln\left(\frac{\theta D_{OL}}{b_c} - 1\right) + \bar{b} + \mathcal{O}(\theta D_{OL} - b_c). \quad (6.14)$$

The lens equation for an aligned source ( $\psi = 0$ ) is

$$\beta(\theta) = 2\pi n, \quad (6.15)$$

where  $n$  counts the number of loops performed by the photon around the black hole. Solving Eq. (6.14) for the angular position of the  $n$ -th relativistic image yields

$$\theta_n D_{OL} = b_c \left[1 + e^{\frac{\bar{b} - 2\pi n}{\bar{a}}}\right]. \quad (6.16)$$

Then, introducing the asymptotic image position  $\theta_\infty = b_c/D_{OL}$ , one recovers the Bozza's formula, namely

$$\theta_n = \theta_\infty \left[1 + e^{\frac{\bar{b} - 2\pi n}{\bar{a}}}\right], \quad (6.17)$$

showing that all relativistic images cluster exponentially close to  $\theta_\infty$ .

Of particular interest is the first relativistic image ( $n = 1$ ), whose position is

$$\theta_1 = \theta_\infty \left[1 + e^{\frac{\bar{b} - 2\pi}{\bar{a}}}\right]. \quad (6.18)$$

Since in GR, the asymptotic image location is

$$\theta_\infty^{\text{GR}} = \frac{6\sqrt{3}GM}{c^2 D_{OL}}, \quad (6.19)$$

which corresponds to the angular radius of the Schwarzschild photon sphere, any deviation in the strong-field coefficients  $\bar{a}$  and  $\bar{b}$  induced by  $f(Q)$  gravity modifies both  $\theta_\infty$  and the exponential clustering of relativistic images.

Finally, let us come back to the EHT data. As we saw above, for M87\* and Sgr A\*, the measured angular diameters are respectively

$$\theta_{d,\text{M87*}} = (42 \pm 3) \mu\text{as}, \quad \theta_{d,\text{SgrA*}} = (48.7 \pm 7) \mu\text{as}.$$

The GR predictions obtained from Eq. (6.19) are

$$\theta_{\infty,\text{M87*}}^0 \simeq 39.68 \mu\text{as}, \quad \theta_{\infty,\text{SgrA*}}^0 \simeq 52.8 \mu\text{as}.$$

Since EHT observations are fully consistent with GR within uncertainties, any modification to the asymptotic image location must satisfy

$$\left| \frac{\Delta\theta_\infty}{\theta_\infty^0} \right| < \frac{\text{EHT uncertainty}}{\theta_{d,\text{GR}}}. \quad (6.20)$$

At the  $2\sigma$  level this implies the bounds

$$\left| \frac{\Delta\theta_\infty}{\theta_\infty^0} \right|_{\text{M87}^*} \lesssim 0.15, \quad \left| \frac{\Delta\theta_\infty}{\theta_\infty^0} \right|_{\text{SgrA}^*} \lesssim 0.26. \quad (6.21)$$

Using the strong-deflection coefficients for Case I and Case II, namely (6.9)-(6.12), and inserting them into expression (6.18), we obtain the constraints on the dimensionless parameters  $\frac{\alpha}{M^{2n-2}}$  summarized in Table V. We find that Case II is constrained significantly more tightly, by roughly three orders of magnitude, comparing to Case I. This reflects the fact that Case II induces much larger corrections to the photon-sphere radius and strong-deflection coefficients, making it far more sensitive to current EHT observations and a promising target for next-generation horizon-scale interferometry.

TABLE V: Constraints on  $\alpha$ -parameter from strong-field deflection and EHT data.

Case	$n$	Source	Upper Bound of	$\frac{\alpha}{M^{2n-2}}$
I	2	M87*	$\lesssim$	30.36
I	2	Sgr A*	$\lesssim$	52.63
I	3	M87*	$\lesssim$	738.92
I	3	Sgr A*	$\lesssim$	1280.79
II	2	M87*	$\lesssim$	0.02812
II	2	Sgr A*	$\lesssim$	0.04875
II	3	M87*	$\lesssim$	0.09494
I	3	Sgr A*	$\lesssim$	0.1646

## VII. CONCLUSIONS

Modified gravity continues to play a central role in addressing open questions in gravitational physics and cosmology, ranging from the nature of dark energy to the ultraviolet completion of General Relativity (GR). Among the various geometric reformulations of gravity, covariant symmetric teleparallel gravity offers a compelling framework in which non-metricity, rather than curvature or torsion, carries the gravitational interaction. The promotion of the non-metricity scalar  $Q$  to a general function  $f(Q)$  enriches the structure of the theory, allowing new phenomenology at both cosmological and astrophysical scales, while preserving second-order field equations. These features make  $f(Q)$  gravity an attractive and well-motivated arena for exploring deviations from GR.

Testing modified gravity requires pushing beyond the weak-field and cosmological limits into the strong-gravity regime, where nonlinear effects become dominant and deviations, if present, can be amplified. Black holes, in particular, serve as exceptional laboratories due to their simplicity, universality, and the extreme curvature near their horizons. The advent of horizon-scale observations such as the EHT images of M87\* and Sgr A\*, measurements of the S2 star orbit around the Galactic Center, and the development of precise strong-lensing

frameworks have opened new pathways for probing gravity in conditions inaccessible by any other means. By combining shadow sizes, photon-sphere properties, periastron precession, and strong-field lensing coefficients, it becomes possible to place simultaneous, independent, and complementary constraints on viable extensions of GR.

In this work, we performed the first unified strong-field analysis of power-law  $f(Q)$  gravity using spherically symmetric black-hole solutions, generated by distinct classes of symmetric affine connections. For each solution, we studied the behavior of null geodesics, we derived analytic expressions for the photon-sphere radius and shadow size, and we calculated strong-lensing observables within the Bozza formalism. We showed that the two families of solutions, labeled here as Case I and Case II, exhibit markedly different sensitivity to the deformation parameter  $\alpha$ , with Case II displaying significantly stronger departures from GR for the same magnitude of  $\alpha$ .

We further confronted these predictions with a broad suite of strong-field observables. The EHT shadow diameters of M87\* and Sgr A\* yield tight bounds on the allowed deviations in the photon-sphere radius; the S2 star precession provides independent and complementary constraints on the same parameter space; and the strong-lensing coefficients  $\bar{a}$  and  $\bar{b}$  impose additional restrictions through the logarithmic structure of the deflection angle. When combined, these probes consistently indicate that Case I solutions remain very close to GR for astrophysical black holes, whereas Case II solutions are significantly constrained, especially for the  $n = 2$  power-law model where deviations become observationally significant.

Looking ahead, the rapidly improving landscape of strong-field observations promises even more decisive tests of  $f(Q)$  gravity. Future EHT campaigns with enhanced arrays, high-frequency imaging, and time-domain capabilities will sharply reduce uncertainties in shadow shapes. Next-generation astrometric missions will measure stellar orbits around Sgr A\* with unprecedented precision, and upcoming facilities such as the ngEHT and space-based interferometers will open access to relativistic images and higher-order lensing effects. On the theoretical side, extending the present analysis to rotating black-hole solutions, dynamical spacetimes, and multi-messenger signatures will allow broader classes of  $f(Q)$  models to be tested. Together, these developments have the potential to transform strong-field astrophysics into a definitive tool for probing non-metricity-based modifications of gravity.

## Acknowledgments

ENS acknowledges the contribution of the LISA CosWG, and of COST Actions CA18108 “Quantum Gravity Phenomenology in the multi-messenger approach” and CA21136 “Addressing observational ten-



- 
- [1] E. N. Saridakis *et al.* [CANTATA], Springer, 2021, [[arXiv:2105.12582](#)].
- [2] S. Capozziello and M. De Laurentis, Phys. Rept. **509**, 167 (2011) [[arXiv:1108.6266](#)].
- [3] A. A. Starobinsky, Phys. Lett. B **91**, 99 (1980).
- [4] A. De Felice and S. Tsujikawa, Living Rev. Rel. **13**, 3 (2010) [[arXiv:1002.4928](#)].
- [5] S. Capozziello, Int. J. Mod. Phys. D **11**, 483-492 (2002) [[arXiv:gr-qc/0201033](#)].
- [6] S. Nojiri and S. D. Odintsov, Phys. Lett. B **631**, 1 (2005). [[arXiv:hep-th/0508049](#)].
- [7] A. De Felice and S. Tsujikawa, Phys. Lett. B **675**, 1-8 (2009) [[arXiv:0810.5712](#)].
- [8] P. Asimakis, S. Basilakos and E. N. Saridakis, Eur. Phys. J. C **84**, no.2, 207 (2024) [[arXiv:2212.12494](#)].
- [9] D. Lovelock, J. Math. Phys. **12**, 498 (1971).
- [10] N. Deruelle and L. Farina-Busto, Phys. Rev. D **41**, 3696 (1990).
- [11] G. W. Horndeski, Int. J. Theor. Phys. **10**, 363-384 (1974).
- [12] F. F. Santos, B. Pourhassan and E. N. Saridakis, Fortsch. Phys. **72**, no.3, 2300228 (2024) [[arXiv:2305.05794](#)].
- [13] F. F. Santos, B. Pourhassan, E. N. Saridakis, O. Sokoliuk, A. Baransky and E. O. Kahya, JHEP **12**, 217 (2025) [[arXiv:2410.18781](#)].
- [14] A. De Felice and S. Tsujikawa, Phys. Rev. D **84**, 124029 (2011) [[arXiv:1008.4236](#)].
- [15] Y. F. Cai, S. Capozziello, M. De Laurentis and E. N. Saridakis, Rept. Prog. Phys. **79**, 106901 (2016). [[arXiv:1511.07586](#) [gr-qc]].
- [16] E. V. Linder, Phys. Rev. D **81**, 127301 (2010) [erratum: Phys. Rev. D **82**, 109902 (2010)] [[arXiv:1005.3039](#) [astro-ph.CO]].
- [17] S. H. Chen, J. B. Dent, S. Dutta and E. N. Saridakis, Phys. Rev. D **83**, 023508 (2011) [[arXiv:1008.1250](#) [astro-ph.CO]].
- [18] G. Kofinas and E. N. Saridakis, Phys. Rev. D **90**, 084044 (2014) [[arXiv:1404.2249](#) [gr-qc]].
- [19] G. Kofinas and E. N. Saridakis, Phys. Rev. D **90**, 084045 (2014) [[arXiv:1408.0107](#) [gr-qc]].
- [20] S. Bahamonde, C. G. Böhm and M. Wright, Phys. Rev. D **92**, no.10, 104042 (2015) [[arXiv:1508.05120](#) [gr-qc]].
- [21] S. Bahamonde and S. Capozziello, Eur. Phys. J. C **77**, no.2, 107 (2017) [[arXiv:1612.01299](#) [gr-qc]].
- [22] C. Q. Geng, C. C. Lee, E. N. Saridakis and Y. P. Wu, Phys. Lett. B **704**, 384-387 (2011) [[arXiv:1109.1092](#) [gr-qc]].
- [23] S. Bahamonde, K. F. Dialektopoulos and J. Levi Said, Phys. Rev. D **100**, no.6, 064018 (2019) [[arXiv:1904.10791](#) [gr-qc]].
- [24] S. Bahamonde, K. F. Dialektopoulos, M. Hohmann and J. Levi Said, Class. Quant. Grav. **38**, no.2, 025006 (2020) [[arXiv:2003.11554](#) [gr-qc]].
- [25] S. Capozziello, M. Caruana, J. Levi Said and J. Sultana, JCAP **03**, 060 (2023) [[arXiv:2301.04457](#) [gr-qc]].
- [26] F. F. Santos and H. Boschi-Filho, [[arXiv:2407.10004](#) [hep-th]].
- [27] F. F. Dos Santos, JHAP **3**, no.1, 1-14 (2022) [[arXiv:2201.02500](#) [hep-th]].
- [28] J. M. Nester and H. J. Yo, Chin. J. Phys. **37**, 113 (1999) [[arXiv:gr-qc/9809049](#)].
- [29] J. Beltrán Jiménez, L. Heisenberg and T. Koivisto, Phys. Rev. D **98** (2018) no.4, 044048 [[arXiv:1710.03116](#) [gr-qc]].
- [30] J. Beltrán Jiménez, L. Heisenberg, T. S. Koivisto and S. Pekar, Phys. Rev. D **101** (2020) no.10, 103507 [[arXiv:1906.10027](#) [gr-qc]].
- [31] F. K. Anagnostopoulos, S. Basilakos and E. N. Saridakis, Phys. Lett. B **822**, 136634 (2021) [[arXiv:2104.15123](#) [gr-qc]].
- [32] R. Lazkoz, F. S. N. Lobo, M. Ortiz-Baños and V. Salzano, Phys. Rev. D **100**, no.10, 104027 (2019) [[arXiv:1907.13219](#) [gr-qc]].
- [33] J. Lu, X. Zhao and G. Chee, Eur. Phys. J. C **79**, no.6, 530 (2019) [[arXiv:1906.08920](#) [gr-qc]].
- [34] S. Mandal, D. Wang and P. K. Sahoo, Phys. Rev. D **102**, 124029 (2020) [[arXiv:2011.00420](#) [gr-qc]].
- [35] N. Frusciante, Phys. Rev. D **103**, no.4, 044021 (2021) [[arXiv:2101.09242](#) [astro-ph.CO]].
- [36] G. N. Gadbail, S. Mandal and P. K. Sahoo, Phys. Lett. B **835**, 137509 (2022) [[arXiv:2210.09237](#) [gr-qc]].
- [37] W. Khylllep, A. Paliathanasis and J. Dutta, Phys. Rev. D **103**, no.10, 103521 (2021) [[arXiv:2103.08372](#) [gr-qc]].
- [38] A. De, T. H. Loo and E. N. Saridakis, JCAP **03**, 050 (2024) [[arXiv:2308.00652](#) [gr-qc]].
- [39] B. J. Barros, T. Barreiro, T. Koivisto and N. J. Nunes, Phys. Dark Univ. **30**, 100616 (2020) [[arXiv:2004.07867](#) [gr-qc]].
- [40] H. Shabani, A. De, T. H. Loo and E. N. Saridakis, Eur. Phys. J. C **84**, no.3, 285 (2024) [[arXiv:2306.13324](#) [gr-qc]].
- [41] N. Dimakis, A. Paliathanasis and T. Christodoulakis, Class. Quant. Grav. **38**, no.22, 225003 (2021) [[arXiv:2108.01970](#) [gr-qc]].
- [42] F. K. Anagnostopoulos, V. Gakis, E. N. Saridakis and S. Basilakos, Eur. Phys. J. C **83**, no.1, 58 (2023) [[arXiv:2205.11445](#) [gr-qc]].
- [43] M. J. Guzmán, L. Järv and L. Pati, limit with different connections," Phys. Rev. D **110**, no.12, 124013 (2024) [[arXiv:2406.11621](#) [gr-qc]].
- [44] C. G. Boiza, M. Petronikolou, M. Bouhmadi-López and E. N. Saridakis, [[arXiv:2505.18264](#) [astro-ph.CO]].
- [45] S. Basilakos, A. Paliathanasis and E. N. Saridakis, Phys. Lett. B **868**, 139658 (2025) [[arXiv:2505.19864](#) [gr-qc]].
- [46] L. Heisenberg, Phys. Rept. **1066**, 1-78 (2024) [[arXiv:2309.15958](#) [gr-qc]].
- [47] W. Wang, H. Chen and T. Katsuragawa, Phys. Rev. D **105** (2022) no.2, 024060 [[arXiv:2110.13565](#) [gr-qc]].
- [48] D. Zhao, Eur. Phys. J. C **82** (2022) no.4, 303 [[arXiv:2104.02483](#) [gr-qc]].
- [49] N. Dimakis, A. Paliathanasis, M. Roumeliotis and T. Christodoulakis, Phys. Rev. D **106** (2022) no.4, 043509 [[arXiv:2205.04680](#) [gr-qc]].
- [50] Y. Yang, X. Ren, B. Wang, Y. F. Cai and E. N. Saridakis, Mon. Not. Roy. Astron. Soc. **533**, no.2, 2232-2241 (2024) [[arXiv:2404.12140](#) [gr-qc]].
- [51] I. Ayuso, M. Bouhmadi-López, C. Y. Chen, X. Y. Chew, K. Dialektopoulos and Y. C. Ong, JCAP **11**, 068 (2025)

- [arXiv:2506.03506 [gr-qc]].
- [52] M. A. Alwan, T. Inagaki, B. Mishra and S. A. Narawade, JCAP **09** (2024), 011 [arXiv:2407.03669 [gr-qc]].
- [53] W. Wang, K. Hu and T. Katsuragawa, Phys. Rev. D **111** (2025) no.6, 064038 [arXiv:2412.17463 [gr-qc]].
- [54] P. Karmakar, S. Haridasu and A. Nishizawa, [arXiv:2508.21054 [gr-qc]].
- [55] P. Karmakar and S. Haridasu, [arXiv:2509.07976 [gr-qc]].
- [56] K. Akiyama *et al.* [Event Horizon Telescope], Astrophys. J. Lett. **875** (2019), L1 [arXiv:1906.11238 [gr-qc]].
- [57] K. Akiyama *et al.* [Event Horizon Telescope], Astrophys. J. Lett. **875** (2019) no.1, L6 [arXiv:1906.11243 [astro-ph.GA]].
- [58] K. Akiyama *et al.* [Event Horizon Telescope], Astrophys. J. Lett. **930** (2022) no.2, L12 [arXiv:2311.08680 [astro-ph.HE]].
- [59] F. Ahmed, H. Ali, Q. Wu, T. Zhu and S. G. Ghosh, Eur. Phys. J. C **85** (2025) no.7, 795.
- [60] A. Övgün and M. Fathi, Nucl. Phys. B **1018** (2025), 117063 [arXiv:2504.04331 [gr-qc]].
- [61] M. Fathi and Y. Sekhmani, Eur. Phys. J. C **85** (2025) no.5, 477 [arXiv:2503.02179 [gr-qc]].
- [62] A. A. Araújo Filho, N. Heidari and I. P. Lobo, [arXiv:2509.11985 [gr-qc]].
- [63] S. H. Xiong, Y. Z. Li, X. M. Kuang and J. Matyjasek, Eur. Phys. J. C **85** (2025) no.10, 1143 [arXiv:2508.03270 [gr-qc]].
- [64] M. Del Piano, S. Hohenegger and F. Sannino, Phys. Rev. D **111** (2025) no.6, 064070 [arXiv:2412.13673 [gr-qc]].
- [65] M. Khodadi, S. Vagnozzi and J. T. Firouzjaee, Sci. Rep. **14** (2024) no.1, 26932 [arXiv:2408.03241 [gr-qc]].
- [66] S. Nojiri and S. D. Odintsov, Phys. Dark Univ. **46** (2024), 101669 [arXiv:2408.05668 [gr-qc]].
- [67] W. Liu, D. Wu and J. Wang, Phys. Lett. B **858** (2024), 139052 [arXiv:2408.05569 [gr-qc]].
- [68] B. Hazarika and P. Phukon, Front. Phys. (Beijing) **20** (2025) no.3, 35201 [arXiv:2410.00606 [gr-qc]].
- [69] W. Liu, D. Wu and J. Wang, JCAP **05** (2025), 017 [arXiv:2407.07416 [gr-qc]].
- [70] K. Nozari, S. Saghaei and A. Mohammadpour, Eur. Phys. J. C **84** (2024) no.8, 778 [arXiv:2407.06393 [gr-qc]].
- [71] J. Sun, Y. Liu, W. L. Qian, S. Chen and R. Yue, Chin. Phys. C **47** (2023) no.2, 025104.
- [72] K. Nozari and S. Saghaei, Eur. Phys. J. C **83** (2023) no.7, 588 [arXiv:2305.17237 [gr-qc]].
- [73] A. A. A. Filho, J. A. A. S. Reis and H. Hassanabadi, JCAP **05** (2024), 029 [arXiv:2309.15778 [gr-qc]].
- [74] A. Uniyal, S. Chakrabarti, M. Fathi and A. Övgün, Annals Phys. **462** (2024), 169614 [arXiv:2309.13680 [gr-qc]].
- [75] C. Escamilla-Rivera and R. Torres Castillejos, Universe **9** (2023) no.1, 14 [arXiv:2301.00490 [astro-ph.CO]].
- [76] M. Khodadi, Nucl. Phys. B **985** (2022), 116014 [arXiv:2211.00300 [gr-qc]].
- [77] N. Heidari, A. A. Araújo Filho, R. C. Pantig and A. Övgün, Phys. Dark Univ. **47** (2025), 101815 [arXiv:2410.08246 [gr-qc]].
- [78] M. Afrin, S. Vagnozzi and S. G. Ghosh, Astrophys. J. **944** (2023) no.2, 149 [arXiv:2209.12584 [gr-qc]].
- [79] R. Shaikh, Mon. Not. Roy. Astron. Soc. **523** (2023) no.1, 375-384 [arXiv:2208.01995 [gr-qc]].
- [80] R. Kumar Walia, S. G. Ghosh and S. D. Maharaj, Astrophys. J. **939** (2022) no.2, 77 [arXiv:2207.00078 [gr-qc]].
- [81] M. Khodadi and G. Lambiase, Phys. Rev. D **106** (2022) no.10, 104050 [arXiv:2206.08601 [gr-qc]].
- [82] I. Banerjee, S. Chakraborty and S. SenGupta, Phys. Rev. D **106** (2022) no.8, 084051 [arXiv:2207.09003 [gr-qc]].
- [83] M. Khodadi, G. Lambiase and D. F. Mota, JCAP **09** (2021), 028 [arXiv:2107.00834 [gr-qc]].
- [84] M. Khodadi and E. N. Saridakis, Phys. Dark Univ. **32** (2021), 100835 [arXiv:2012.05186 [gr-qc]].
- [85] M. Khodadi, A. Allahyari, S. Vagnozzi and D. F. Mota, JCAP **09** (2020), 026 [arXiv:2005.05992 [gr-qc]].
- [86] S. Vagnozzi, C. Bambi and L. Visinelli, Class. Quant. Grav. **37** (2020) no.8, 087001 [arXiv:2001.02986 [gr-qc]].
- [87] S. Vagnozzi and L. Visinelli, Phys. Rev. D **100** (2019) no.2, 024020 [arXiv:1905.12421 [gr-qc]].
- [88] A. Allahyari, M. Khodadi, S. Vagnozzi and D. F. Mota, JCAP **02** (2020), 003 [arXiv:1912.08231 [gr-qc]].
- [89] O. Y. Tsupko, Z. Fan and G. S. Bisnovatyi-Kogan, Class. Quant. Grav. **37** (2020) no.6, 065016 [arXiv:1905.10509 [gr-qc]].
- [90] F. D'Ambrosio, S. D. B. Fell, L. Heisenberg and S. Kuhn, Phys. Rev. D **105** (2022) no.2, 024042 [arXiv:2109.03174 [gr-qc]].
- [91] C. Bambi, K. Freese, S. Vagnozzi and L. Visinelli, Phys. Rev. D **100** (2019) no.4, 044057 [arXiv:1904.12983 [gr-qc]].
- [92] S. Vagnozzi, R. Roy, Y. D. Tsai, L. Visinelli, M. Afrin, A. Allahyari, P. Bambhaniya, D. Dey, S. G. Ghosh and P. S. Joshi, *et al.* Class. Quant. Grav. **40** (2023) no.16, 165007 [arXiv:2205.07787 [gr-qc]].
- [93] R. Abuter *et al.* [GRAVITY], Astron. Astrophys. **636** (2020), L5 [arXiv:2004.07187 [astro-ph.GA]].
- [94] R. Abuter *et al.* [GRAVITY], Astron. Astrophys. **657** (2022), L12 [arXiv:2112.07478 [astro-ph.GA]].
- [95] K. S. Virbhadra and G. F. R. Ellis, Phys. Rev. D **65** (2002), 103004.
- [96] S. Frittelli, T. P. Kling and E. T. Newman, Phys. Rev. D **61** (2000), 064021 [arXiv:gr-qc/0001037].
- [97] V. Bozza, Phys. Rev. D **66** (2002), 103001 [arXiv:gr-qc/0208075].